

## Microfluid Switching-Induced Transient Refractive Interface

Jiukai Tang, Guangyu Qiu, Xiaobao Cao, Andrew deMello, and Jing Wang\*

Cite This: *ACS Sens.* 2022, 7, 3521–3529

Read Online

ACCESS |



Metrics &amp; More



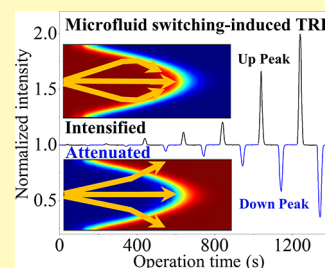
Article Recommendations



Supporting Information

**ABSTRACT:** The laminar flow interface (LFI) developed at low Reynolds numbers is one of the most prominent features of microscale flows and has been employed in a diverse range of optofluidic applications. The formation of LFIs usually requires the manipulation of multiple streams within a microchannel using a complex hydrodynamic pumping system. Herein, we present a new type of LFI that is generated by fluid switching within a three-dimensional (3D) microlens-incorporating microfluidic chip (3D-MIMC). Since Poiseuille flows exhibit a parabolic velocity profile, the LFI is cone-like in shape and acts as a transient refractive interface (TRI), which is sensitive to the refractive index (RI) and the Péclet number ( $Pe$ ) of the switching fluids. In response to the TRI, the intensity of the transmitted light can be intensified or attenuated depending on the sequence of fluid switching operations. By incorporating three-dimensional (3D) microlenses and increasing the  $Pe$  values, the profile and amplitude of the intensity peak are both significantly improved. The limit of detection (LoD) for a sodium chloride (NaCl) solution at  $Pe = 1363$  is as low as 0.001% (w/w), representing an improvement of 1–2 orders of magnitude when compared to existing optofluidic concentration sensors based on intensity modulation. Fluid switching of a variety of inorganic and organic sample fluids confirms that the specific optical response ( $K_{or}$ ) correlates positively with both  $Pe$  and the specific RI ( $K_{nc}$ ), obeying a linear relationship. This model is further verified through cross-validations and used to estimate the molecular diffusion coefficient ( $D$ ) of a range of species. Furthermore, by virtue of the TRI, we achieve a sensitive measurement of optical-equivalent total dissolved solids (OE-TDS) for environmental samples.

**KEYWORDS:** laminar flow interface, microfluid switching, refractive index, diffusion coefficient, Poiseuille flow



The laminar flow interface (LFI) at low Reynolds numbers is one of the most important features of microscale flows.<sup>1–3</sup> LFIs have been used to develop novel methods for microfabrication<sup>4–7</sup> and cell patterning.<sup>8</sup> Additionally, a variety of optofluidic functions, originating from the difference of fluid properties on each side of the LFI and the LFI geometry, have been realized and used to monitor chemical reactions<sup>9</sup> and perform optical modulations via prisms,<sup>10</sup> microlenses,<sup>11,12</sup> and waveguides.<sup>13</sup> Normally, the LFIs are formed in microfluidic systems by the simultaneous pumping and manipulation of multiple streams.<sup>14,15</sup> For example, Yang et al. pumped two cladding fluids and one core fluid within a microchannel to form an LFI for transformation optics.<sup>16</sup> In another study, two centrifugal Dean flow streams were generated within a curved microchannel to form a three-dimensional (3D) LFI, with a view to improving the confinement of light in high-efficiency dye lasers.<sup>17</sup> Despite the obvious utility of LFIs, the need for complex fluidic control of multiple streams has limited their use and application. To this end, we present a new type of 3D LFI, naturally developed in a Poiseuille flow within a 3D-microlens-incorporating microfluidic chip (3D-MIMC). Poiseuille flow is a basic feature in microscale flow, where a parabolic velocity profile is developed in the plane perpendicular to the flow direction<sup>18</sup> and described by the convection–diffusion eq 1.

$$\partial c / \partial t = D \nabla^2 c - \mathbf{v} \cdot \nabla c \quad (1)$$

Here,  $c$  is a concentration variable,  $D$  is the molecular diffusion coefficient,  $\mathbf{v}$  is the velocity vector, and  $\nabla c$  is the concentration gradient. For Poiseuille flows at high  $Pe$  values, convection rather than diffusion dominates mass transport and thus a cone-like LFI will appear between the coming and leaving fluids (schematically shown in Figure 1a).  $Pe$  is defined as the ratio of the advective transport rate to the diffusive transport rate, as shown in eq 2.<sup>16,19</sup>

$$Pe = \frac{UL}{D} \quad (2)$$

where  $Pe$  is the Péclet number;  $U$  is the average velocity of the switching fluid;  $L$  is the characteristic length ( $L = 0.25$  mm in this work, equal to the width of the detection channel); and  $D$  is the molecular diffusion coefficient of solutes in the switching fluid.

The LFIs developed in Poiseuille flows can be used for optofluidic applications. Optofluidic concentration sensors are widely used in industrial metrology, biochemical analysis, and environmental monitoring.<sup>20–27</sup> For example, advanced

Received: August 30, 2022

Accepted: October 31, 2022

Published: November 10, 2022



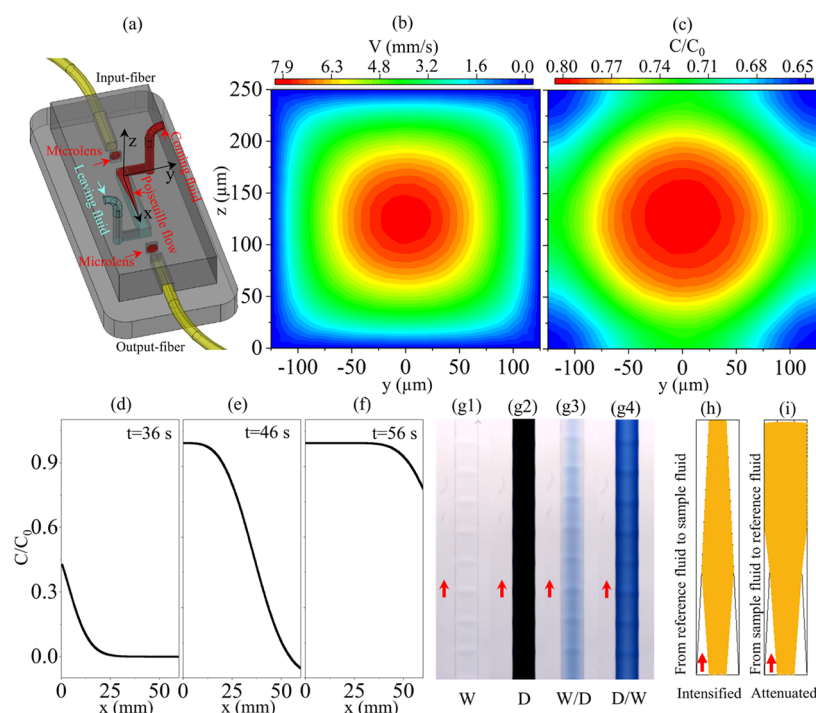


**Figure 1.** (a) Schematic of microfluidic switching within a 3D-MIMC. (b) Velocity field of a fully developed Poiseuille flow. (c) Concentration field ( $x = 30$  mm,  $t = 46$  s). The evolutionary concentration profiles along the channel centerline ( $y = 0$   $\mu\text{m}$ ,  $z = 125$   $\mu\text{m}$ ). (d)  $t = 36$  s, (e)  $t = 46$  s, and (f)  $t = 56$  s.  $t = 0$  s corresponds to the time fluid entering the peristaltic tubing.  $C_0$  is the concentration of the sample fluid in the steady state. Steady and transient states are illustrated using ultrapure water and the dye solution. (g1) Ultrapure water filled in the channel (W), (g2) the dye solution filled in the channel (D), (g3) fluid switched from ultrapure water to the dye solution (W/D), and (g4) fluid switched from the dye solution to ultrapure water (D/W). Arrows in (g1–g4) represent the flow direction. Simulated optical responses caused by the TRI during fluid switching. (h) Switching from the reference fluid to the sample fluid and (i) switching from the sample fluid to the reference fluid. In this work, the  $RI$  of the sample fluid is higher than that of the reference fluid. Arrows in (h) and (i) represent the directions of both flow and light propagation. The flow direction and light propagation direction are the same in this work.

photonic structures involving photonic crystal fibers (PCFs), ring resonators, Fabry–Pérot microcavities, and surface plasmon resonance (SPR) configurations have been employed as wavelength modulation-based optofluidic  $RI$  sensors for the measurement of salinity and glucose content.<sup>28–31</sup> Despite the excellent analytical performance, complicated fabrication protocols and the need for high-resolution spectrometers limit their applications. To address this issue, Weber et al. developed an intensity modulation-based optofluidic sensor that simply depends on total internal reflection (TIR). Unfortunately, the limit of detection (LoD) for a calcium chloride ( $\text{CaCl}_2$ ) solution was calculated as only 0.44% (w/w).<sup>32</sup> Additionally, in a more recent study by Tang and co-workers, an LoD of 0.04% (w/w) NaCl was achieved using a 3D-microlens-cascade optofluidic chip.<sup>33</sup> Although this development yields a significant improvement in performance for the intensity modulation-based optofluidic  $RI$  sensors, it is still extremely difficult to probe solution concentrations at or lower than the 0.001% (w/w) scale, which is the norm in a range of quality control applications in water process and production industries. In addition to measuring solution concentrations, the molecular diffusion coefficient ( $D$ ) is a parameter of much interest in optofluidic applications. For example, Zhao et al. measured the diffusion coefficients of ethylene glycol and glycerol in water using the LFI in a microchannel through a focus shift.<sup>9</sup> Taylor dispersion analysis (TDA) of Poiseuille flows has also been used to measure molecular diffusion coefficients.<sup>18,34</sup> In TDA, high-resolution ultraviolet (UV) and  $RI$  detectors are used to measure the peak broadening of a

solute plug in a Poiseuille flow. As aforementioned in the last paragraph, a Poiseuille flow itself presents a parabolic velocity profile, enabling a naturally formed 3D LFI between the coming and leaving fluids. Such an LFI can act as a transient refractive interface (TRI), which is sensitive to both the  $RI$  and  $Pe$  of switching fluids. This means that for a given flow velocity, both the solution concentrations and the molecular diffusion coefficient can be derived.

In the current study, we characterize a TRI during fluid switching operations through both experiment and simulation. The optical responses to the TRI are analyzed in terms of the peak profile and sensitivity. Furthermore, a binary regression analysis is used to understand the correlation of the optical response with both the  $RI$  and  $Pe$ . The correlation model is further evaluated through cross-validations for estimating  $D$  values. Additionally, we investigated the application of the TRI in the measurement of optical-equivalent total dissolved solids (OE-TDS) and differentiating compositions in different environmental matrices.

## EXPERIMENTAL SECTION

**Chip Fabrication and System Configuration.** The system consists of a white LED (MNWHD2, Thorlabs), bare optical fibers (FG105UCA, Thorlabs), a 3D-microlens-incorporating microfluidic chip (3D-MIMC), a spectrometer (ULS2048LTEC, Avantes, Netherlands), and a peristaltic pump (REGLO Digital MS-4/6, ISMATEC, Germany). As shown in Figure 1a, all optical elements in the 3D-MIMC including the fiber grooves, the microlens cavities (the microlens: diameter = 0.25 mm, thickness = 0.025 mm), and the detection channel (length  $\times$  width  $\times$  height = 60 mm  $\times$  0.25 mm  $\times$

0.25 mm) are self-aligned within the chip. The 3D-MIMC is easily reproduced via mold replication using poly(dimethylsiloxane) (PDMS). The optical fibers are inserted into their grooves with the end faces at the focal point of the microlens. The microlenses are self-incorporated as an optofluidic cavity during PDMS replication to conveniently characterize their performances by replacing the filling in the cavity. In this study, the microlens effect is eliminated by replacing the original air filling ( $RI = 1.00$ ) with a 50% (w/w) glucose solution ( $RI = 1.41$ , identical to that of the chip material, PDMS). The detailed fabrication process can be found in our previously published work.<sup>35,36</sup> The coming and leaving fluids during switching operations are schematically shown in Figure 1a. For the switching operation, after stopping the peristaltic pump, the tubing end is moved from one fluid, cleaned, and immersed into the other fluid. Afterward, the peristaltic pump is restarted immediately. In this configuration, a one-channel peristaltic pump is sufficient.

**Velocity Profile of Laminar Flow.** The modules of laminar flow and transport of diluted species in COMSOL were used to depict the velocity and concentration profiles during microfluid switching in a channel. Ray tracing module was additionally used to schematically depict the optical responses. In the simulation of the velocity profile, the average flow rate at the inlet (internal diameter: 130  $\mu\text{m}$ ) and the pressure at the outlet were set as 16.5  $\mu\text{L min}^{-1}$  and 0 Pa, respectively. The reference fluid and sample fluid were represented by ultrapure water and 1% (w/w) NaCl solution. The molecular diffusion coefficient ( $D$ ) of NaCl in water was set as  $1.6 \times 10^{-9} \text{ m}^2 \text{ s}^{-1}$ .

**Samples and Analytical Methods.** Analytical-grade reagents including sodium chloride (NaCl, Sigma), potassium chloride (KCl, Sigma), calcium chloride ( $\text{CaCl}_2$ , Sigma), magnesium sulfate ( $\text{MgSO}_4$ , Sigma), ammonium chloride ( $\text{NH}_4\text{Cl}$ , Sigma), glucose (Sigma), urea (Sigma), and ethanol (VWR) were prepared as solution samples in ultrapure water. The prepared sample concentrations are in the range of 0.001–2% (w/w) for the characterization of the optical responses to the TRI and in the range of 0.5–20% (w/w) for the characterization of  $RI$  responses. All solution samples were loaded using the peristaltic pump at flow rates 8.5–63.5  $\mu\text{L min}^{-1}$ . According to the flow velocity, the characteristic length of the microchannel and  $D$  and  $Pe$  can be calculated. All experiments were implemented three times to check the reproducibility at  $24.5 \pm 1.0^\circ\text{C}$ . The optical responses to microfluid switching are defined as eq 3.  $RI$  responses to the change of microlens cavity filling are defined as eq 4.

$$\text{optical response} = \lg \left| \frac{I_{\text{reference-TRI}}}{I_{\text{peak-TRI}}} \right| \quad (3)$$

where optical response is a dimensionless parameter with an arbitrary unit (AU);  $I_{\text{reference-TRI}}$  is the light intensity recorded by the spectrometer corresponding to the case of the reference fluid (ultrapure water in this study) filled in the detection channel; and  $I_{\text{peak-TRI}}$  is the spike value of the light intensity recorded by the spectrometer during the switching between the reference fluid and the sample fluid in the detection channel. Since the light intensity of the optical response can be higher or lower than the reference intensity, an absolute expression is used.

$$RI \text{ response} = \lg \frac{I_{\text{reference-RI}}}{I_{\text{peak-RI}}} \quad (4)$$

where  $RI$  response is a dimensionless parameter with an arbitrary unit (AU) and  $I_{\text{reference-RI}}$  and  $I_{\text{peak-RI}}$  are the light intensities recorded by the spectrometer corresponding to the microlens cavities filled with ultrapure water and sample solutions, respectively.

The water samples were taken from the rivers and the public drinking network in Zurich. These raw water samples were filtered using a cellulose acetate membrane (pore size 0.45  $\mu\text{m}$ ) before optical measurements. The membrane was rinsed twice using ultrapure water prior to filtration. The aerosol samples were from the Swiss National Air Pollution Monitoring Network. The aerosol samples were collected using quartz fiber filters. The filter was cut into pieces and immersed in 5 mL of water, followed by shaking at a speed of 1200

rpm for 120 min. Afterward, the elute was separated by centrifugation at 3500 rpm for 10 min. The eluate was diluted 10 times before optical measurements. The OE-TDS for environmental samples is defined as the concentration of NaCl solutions leading to the same optical responses.

**Cross-Validation.** NaCl was used as the calibration sample for the measurement of the specific refractive index ( $K_{nc}$ ). A cross-validation was implemented for the  $D$  value derivation. In the cross-validation, the parameters including  $K_{nc}$ ,  $D$ , and the measured (the sensitivity of optical responses to the TRI)  $K_{or}$  of training samples were employed to establish the linear model, while the remaining one acted as the test sample.

## RESULTS AND DISCUSSION

**Microfluid Switching-Induced TRI.** Figure 1a schematically shows the configuration of the 3D-MIMC and a Poiseuille flow in the microchannel. Detailed descriptions are included in the Experimental Section. The actual fabricated chip, the magnified part of the detection channel and the microlens cavity, and the scanning electron microscopy (SEM) image of the microlens are shown in the Supporting Information (Figure S1a,b,c). Figure 1b shows the simulated velocity profile, in which the velocity is the largest and zero at the channel cross-section center and boundary, respectively, obeying the characteristics of a Poiseuille flow.<sup>37</sup> At a high  $Pe$  value, the velocity profile of the Poiseuille flow induces a clear concentration profile in the channel during switching of two different fluids since the convection process is much more predominant than the diffusion process. As shown in Figure 1c, at  $x = 30 \text{ mm}$  and  $t = 46 \text{ s}$ , the relative concentration at the channel cross-section center is clearly higher than that of its surroundings. Figure 1d–f shows the evolution of the concentration profile along the channel centerline ( $y = 0 \mu\text{m}$ ,  $z = 125 \mu\text{m}$ ). At  $t = 36 \text{ s}$ , the concentration profile is not well developed to cover the entire channel since the sample fluid just entered the channel. At  $t = 46 \text{ s}$ , the head of the fluid just leaves the channel, and the concentration gradient covers almost the entire channel. The concentration profile evolves as a cone-like profile within the  $xy$  plane at  $z = 125 \mu\text{m}$  and functions as an optimal TRI to induce intensive optical responses, as shown in the Supporting Information (Figure S2). At  $t = 56 \text{ s}$ , the concentration gradient gradually faded away through the diffusion process, and the entire channel turned almost saturated. Besides the simulation, images were captured as well to illustrate the process of fluid switching. Figure 1g1,g2 presents the steady states in which ultrapure water and the dye solution are filled in the detection channel, respectively. In these two steady states, no LFI, concentration profile, and TRI exist. In contrast, Figure 1g3,g4 indicates the developed LFI and concentration profiles as a result of the mutual switching between ultrapure water and the dye solution. The optical responses to the TRI are schematically represented using the ray optics module in COMSOL. Figure 1h shows the optical responses to the TRI during switching the reference fluid to the sample fluid, in which the divergence of light can be corrected, leading to an enhanced intensity of light collected by the spectrometer. Conversely, in Figure 1i, since the TRI is induced by the switching from the sample fluid to the reference fluid, the divergence of light can be extended, causing an intensity attenuation of the transmitted light.

**Up and Down Peaks as the Optical Responses to the TRI.** As the optical responses to microfluid switching, up and down peaks appear depending on the sequence of fluid switching (Figure 2a). The inset plot is the magnified part of



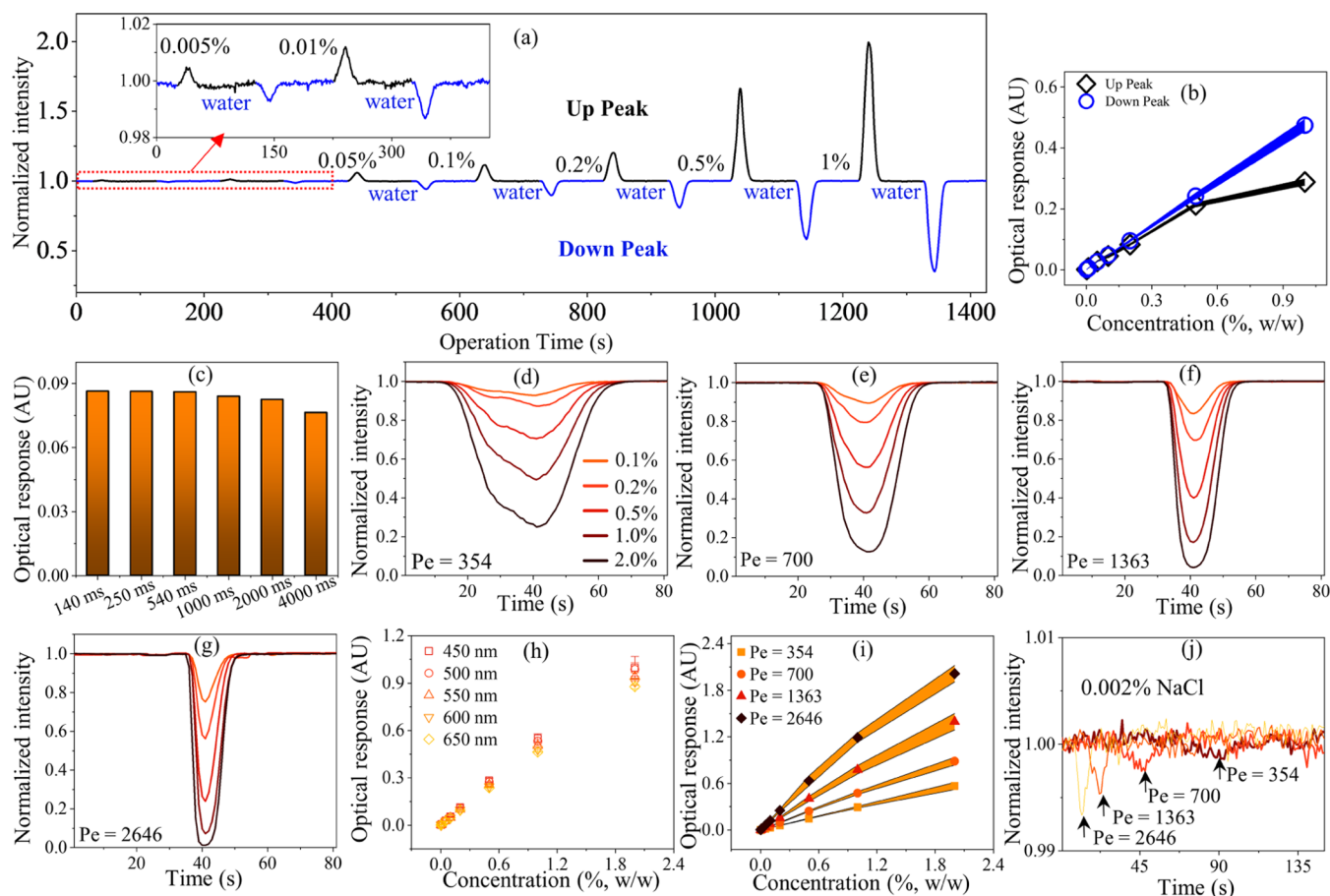


**Figure 2.** (a) Real-time optical responses to the microfluidic switching between the reference fluid (ultrapure water) and the sample fluid (NaCl solution, 0.005–1%, w/w) within 3D-MIMC at  $Pe = 700$ . The intensity is normalized by the average intensity detected when ultrapure water is filled in the detection channel. (b) Relationship between the optical response and the sample concentration derived from the up peak and the down peak at  $Pe = 700$ . (c) Optical responses measured with different time resolutions to the switching from 0.1% (w/w) NaCl to ultrapure water at  $Pe = 1363$ . (d–g) Peak profiles at different  $Pe$  values for the fluid switching from NaCl solutions to ultrapure water. (h) Effects of wavelength on the sensitivity of optical responses at  $Pe = 700$ . (i) Effects of  $Pe$  values on the sensitivity of optical responses. (j) Enhanced capability of detecting a 0.002% (w/w) NaCl solution at high  $Pe$  values.

the optical responses to the switching between ultrapure water and NaCl solutions at low concentrations of 0.005 and 0.01% (w/w). When the fluid in the detection channel is switched from ultrapure water to NaCl solutions, the TRI functions as a waveguide to intensify the light collection and leads to the up peak due to the RI difference between these two fluids. On the contrary, when the fluid is switched from NaCl solutions to ultrapure water, the TRI functions as a light attenuator and leads to the down peak. The effects of the microlens on the characteristics of the optical responses were investigated. Figure S3a in the Supporting Information presents the results without microlenses; the peak profiles of the optical responses are irregular due to the appearance of secondary peaks. Additionally, no significant linear relationship between the up peak-based optical responses and the sample concentration can be established. Some data points (for example, at the concentration 0.05% (w/w) in Figure S3b in the Supporting Information) of the down peak-based optical response deviate despite the improvement of the linear relationship. In contrast, the optical responses in Figure 2a are always regular in profiles thanks to the incorporation of 3D microlenses and increase with the sample concentration, implying an excellent capability of the TRI for analyzing solution properties. The optical responses are compared in terms of sensitivity and linear

dynamic range (Figure 2b). A second-order polynomial curve fitting was employed for the regression analysis. The sensitivities represented by the slope values of the optical response curves for the up and down peaks are almost the same within the NaCl concentration range of less than 0.5% (w/w). The linear dynamic range is determined as the region between the LoD and the point where the contribution of the quadratic term starts to exceed 5% of the linear term. The data points based on the up peak deviate from the linear relationship for concentrations higher than 0.2% (w/w), while the curve derived from the down peak keeps a good linear relationship within a broader concentration range (0.002–1.1%, w/w). Additionally, the measurement of the down peak can prevent detector saturation and ensure the safe operation of the device. Therefore, the down peak is selected for sample characterization. Since fluid switching is a transient process, the time resolution of the optical response was additionally investigated. Figure S4a–f in the Supporting Information shows the real-time optical responses measured with different time resolutions within a 1 min operation. The optical responses with time resolutions ranging from 140–2000 ms show a minor coefficient of variation ( $CV = 2\%$ ), while a 10% drop in the optical response is observed with a time resolution equal to 4000 ms, as shown in Figure 2c. To

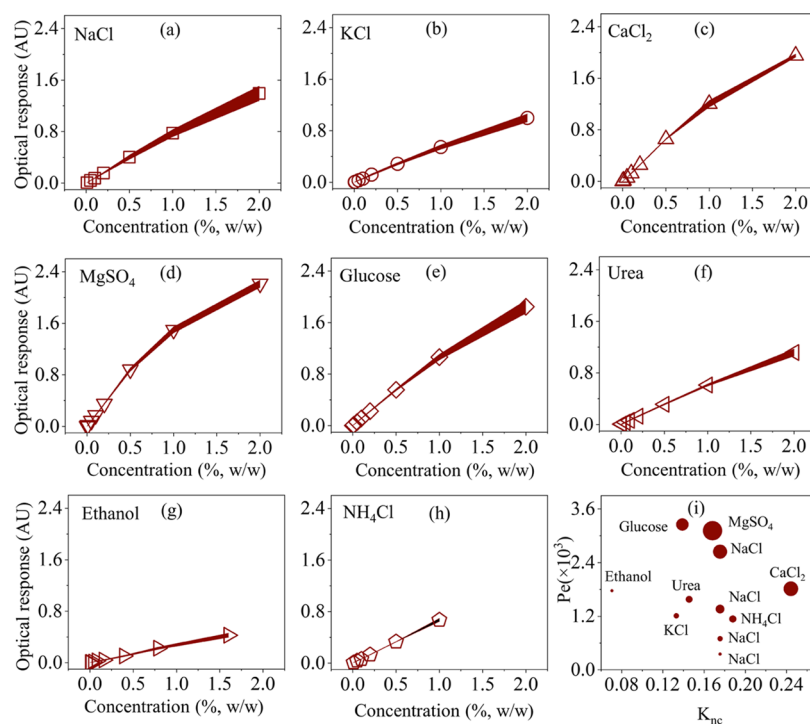


**Figure 3.** (a–h) Optical responses to the fluid switching from a variety of samples to ultrapure water. (i) Combined contributions of  $K_{nc}$  and  $Pe$  to the optical responses. The area of bubbles in Figure 3i represents the slope value of the linear regression curve between the optical response and sample concentration, while  $K_{nc}$  is the slope of the linear regression curve between the RI and the sample concentration (w/w). All data of RI and  $D$  are the values at 25 °C gathered from published papers.<sup>38–49</sup>

prevent data redundancy and achieve a sufficient resolution, 1000 ms is selected in this study to capture the dynamic features of microfluidic switching.

**Peak Profiles at Different  $Pe$  Values.** Peak profiles change with  $Pe$  values. Figure 2d–g shows the optical responses to the switching from NaCl solutions to ultrapure water at four  $Pe$  values. When increasing the  $Pe$  value from 354 to 2646, the mean peak width is narrowed from 55 to 19 s. The peak width is defined as the range within which the intensity is lower than the threshold value (three times of standard deviation of the baseline noise subtracted from the baseline level). The width of the first half peak is slightly higher than the retention time of the sample fluid in the detection channel. This suggests that the optical response starts when the central head of the incoming fluid arrives at the entrance of the detection channel and then develops to the highest level shortly after the central head leaves the exit of the detection channel. Afterward, the optical response gradually attenuates and eventually disappears after the concentration profile-induced TRI vanishes. According to Figure 2d–g, the peak profiles present a high similarity at the same  $Pe$  value, while the width ratio of the first half peak and the second half peak decreases from 1.1 to 0.4 when increasing the  $Pe$  value from 354 to 2646. The widths of the first half peak and the second half peak represent the two subranges of the peak width split by the minimum point.

**Sensitivity at Different Wavelengths and  $Pe$  Values.** Sensitivity enhancement is critical to improving analytical performance in solution concentration measurement. In this study, we investigated the effects of light wavelength and the  $Pe$  value on the sensitivity of the optical responses. Figures 2h and S5 in the Supporting Information present the optical responses at different wavelengths and the real-time intensity variations

within a wavelength range (420–720 nm) during the fluid switching between ultrapure water and the 0.1% (w/w) NaCl solution. The optical response at 450 nm is approximately 18% more sensitive than that at 650 nm, which can be attributed to the dependence of the RI on light wavelength. That said, considering the availability of literature RI values at 589 nm (corresponding to the emission wavelength of sodium lamp), 589 nm is selected for sample quantifications in this study. Compared to light wavelength, the sensitivity is more susceptible to  $Pe$  values. When increasing the  $Pe$  value from 354 to 2646, the sensitivity improves almost 5 times, as shown in Figure 2i. Correspondingly, the capability of quantifying low concentrations of samples increases. As shown in Figure 2j, for the 0.002% (w/w) NaCl solution, the signal is almost indistinguishable from the noise at  $Pe = 354$ . After increasing the  $Pe$  value, a clear separation of signal from noise is observed. Although a larger  $Pe$  value may lead to a higher sensitivity, the linear dynamic range can be narrower, as shown in the Supporting Information (Table S1). Additionally, a high rotation speed of the pump rotator is needed to reach a high  $Pe$  value, which can accelerate the abrasion of the tubing wall and affect the system's stability in a long-term operation.

**Combined Contribution of  $K_{nc}$  and  $Pe$ .** We investigated the optical responses to the TRI between the reference fluid (ultrapure water) and a variety of sample fluids, including inorganic salt solutions and organic solutions. A set of significant linear relationships between the optical response and the solution concentration have been established for all of the samples despite the difference in slope values. As shown in Figure 3a–h, the sensitivity for magnesium sulfate ( $MgSO_4$ ) proves to be the highest among the investigated samples, which is almost 7 times higher than that of the ethanol solution. Such a sensitivity difference is attributed to two critical factors: the

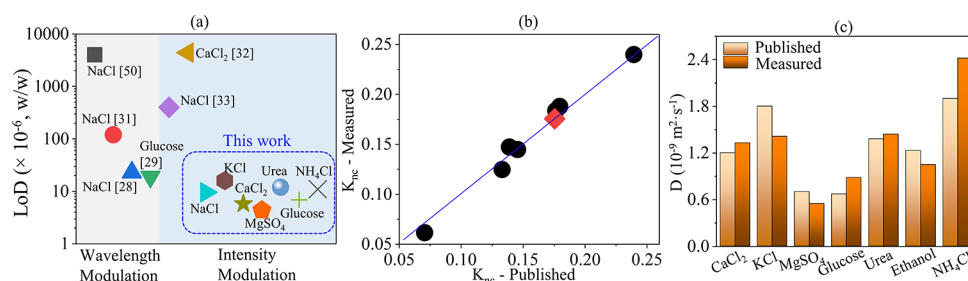


**Figure 4.** (a) Result comparison from aspects of transduction mechanisms and the LoD. (b) Excellent consistency between the published  $K_{nc}$  and the measured  $K_{nc}$  using the microlens cavity. The red data point represents NaCl as the calibration substance. (c) Comparable  $D$  values published and measured in this study.

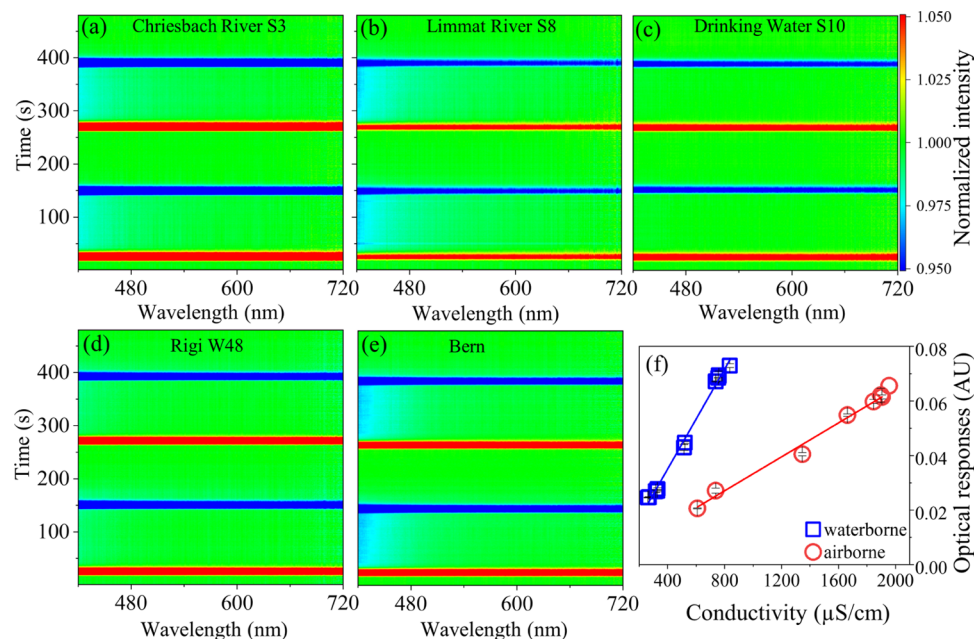


**Figure 5.** Two cycles of intensity variations to the switching between ultrapure water and different environmental samples, (a), (b), and (c) Waterborne samples from Chriesbach River, Limmat River, and the public drinking network in Zurich. (d) and (e) Water extractable matter in aerosol samples collected at Rigi station and Bern station in the Swiss National Air Monitoring System. (f) Relationship between the optical response and the conductivity of the environmental samples.

specific  $RI(K_{nc})$  and  $Pe$  values.  $K_{nc}$  is defined as the sensitivity of  $RI$  to the mass concentration of solution samples. The combined effect of  $K_{nc}$  and  $Pe$  is shown in Figure 3i, in which the area of bubbles represents the slope value ( $K_{or}$ ) of the linear regression curve between the optical response and sample concentration. Through a binary linear regression, a significant linear relationship has been founded among  $K_{or}$ ,  $K_{nc}$ , and  $Pe$ , with the  $R$ -square value equal to 0.93, as described in eq 5. It clearly reveals that those sample fluids with higher  $K_{nc}$  and  $Pe$  values can lead to more sensitive optical responses to the TRI. According to the regression relationship, the predicted and measured  $K_{or}$  values are well matched with a mean error of  $7.8 \pm 5.6\%$ , as shown in the Supporting Information (Figure S6).

$$K_{or} = -97.9 + 644.8 \cdot K_{nc} + 0.046 \cdot Pe \quad (5)$$

#### Versatile Measurement of Solution Properties.

Noticeably, the 3D-MIMC possesses versatile capabilities, including ultrasensitive solution concentration quantification,  $RI$  measurement, and the estimation of  $D$  values. The specific configurations for characterizing the optical response to the TRI (transient state in the detection channel) and the  $RI$

responses (steady state in the microlens cavity) are shown in the Supporting Information (Figure S7a,b). An ultralow LoD for solution concentration quantification through the TRI has been demonstrated. The results from this study and those by other researchers are compared in Figure 4a and Table S2 in the Supporting Information. From the aspect of fabrication, Weber's and our sensors have the advantage that the detection can be implemented within microchannels without the need for complicated optical configurations.<sup>32</sup> However, the LoD of Weber's solution sensor is only 0.44% (w/w) for a CaCl<sub>2</sub> solution, requiring further improvements for sensitive applications. In contrast, the LoD for the CaCl<sub>2</sub> solution in our work is 0.0006% (w/w), almost three orders of magnitude lower. Since the quantification metric of our sensor is intensity variations instead of wavelength shifts,<sup>28,29,31,50</sup> the spectrometer can be replaced by a photodiode toward a miniaturized and low-cost analysis system. Besides solution concentration quantification,  $RI$  measurement is realized as well since the convergence of light through the input and output microlens cavities is sensitive to the filled liquid  $RI$ . Consequently, the sample  $K_{nc}$  can be calculated according to the calibration curve. Specifically, we employed NaCl solutions to establish the  $RI$



calibration curve. As shown in the Supporting Information (Figure S8a), the stepwise change curve of light intensity is observed, which results from the concentration variations in the microlens cavity. The intensity change is converted to the RI calibration curve, as shown in the Supporting Information (Figure S8b). Figure S8c–i in the Supporting Information shows the RI responses for different test sample solutions. The  $K_{nc}$  values can be obtained according to the calibration curve in the Supporting Information (Figure S8b). As shown in Figure 4b, the measured and published  $K_{nc}$  values are almost the same. Combining  $K_{nc}$ ,  $K_{or}$ , the flow velocity, and the channel dimension, the derived  $D$  values are presented in Figure 4c with a mean error of  $19 \pm 10\%$  through cross-validations. The results of cross-validations, including the test sample set, the training sample set, the established model, and  $R$ -square values, are provided in the Supporting Information (Table S3).

**Measurements of Environmental Samples.** Total dissolved solids (TDS) is a critical index in the environmental analysis and desalination industry, conventionally measured by a weighing method or represented by conductivity as a fast measurement. That said, the weighing method is time-consuming, and volatile compounds normally cannot be taken into account due to evaporation loss. For the conductivity method, correction factors have to be added in analyzing different categories of samples.<sup>51</sup> Additionally, since some organic substances (e.g., glucose) are nonionizable and cannot be measured by the conductivity-based method, TDS might be underestimated. In this study, we exploited the TRI as a new optical supplementary assay to characterize the OE-TDS in different environmental samples. As shown in the Supporting Information (Table S4), the mean OE-TDS in river water is higher than that in public drinking water, while the airborne samples from Rigi station and Bern station have comparable mean OE-TDS. Figure 5a–e presents the optical responses to the switching between ultrapure water and the environmental sample fluids. Although some waterborne and airborne samples (sampling information described in the Methods section) exhibit strong absorption in the blue region, the light intensity at 589 nm is not affected and is still valid to calculate the optical responses. By a combined use of the TRI method and the conductivity method, the waterborne and airborne environmental samples are grouped into two clusters. Two linear relationships between the optical responses and conductivity are well established, as shown in Figure 5f. It suggests a significant composition difference of dissolved matter between the waterborne and airborne samples as well as a high composition similarity in the local water and air environment despite concentration variations.

## CONCLUSIONS

In this work, we have studied the fundamental characteristics of the transient phenomenon during microfluid switching, including the velocity profile, mass transfer, and effects on optical responses. The LFI naturally develops in a Poiseuille flow during microfluid switching within a 3D-MIMC and acts as a TRI. During fluid switching, both up peak and down peak can appear depending on the switching sequence. The results indicate the optical responses are highly sensitive to both the RI and  $Pe$  values of microfluids. High  $Pe$  and  $K_{nc}$  can lead to a high  $K_{or}$ . At  $Pe = 1363$ , the LoD for NaCl solution concentration quantification is calculated as 0.001% (w/w), representing an excellent performance through intensity modulation. A significant linear relationship is established

among  $K_{or}$ ,  $K_{nc}$ , and  $Pe$ . According to this model,  $D$  values can be derived after obtaining  $K_{nc}$  using the microlens cavity within the same chip. The fluid switching operation within the 3D-MIMC provides a simple method for the characterization of multiple material properties. Furthermore, we have employed the TRI to analyze waterborne and airborne environmental samples, demonstrating its potential in quantifying and differentiating dissolved matter originating from different matrices. We envision more applications of the TRI within the 3D-MIMC in industrial metrology, water purification, and environmental monitoring.

## ASSOCIATED CONTENT

### Supporting Information

The Supporting Information is available free of charge at <https://pubs.acs.org/doi/10.1021/acssensors.2c01901>.

Description of the chip configuration and tubing connection; description of the concentration profile in the xy plane; the effects of microlens, time resolution and wavelength on optical responses; relevant information of the modelling and cross-validation; comparison with other optofluidic systems; OE-TDS data calculated for waterborne and airborne samples. (PDF)

## AUTHOR INFORMATION

### Corresponding Author

Jing Wang – Institute of Environmental Engineering, ETH Zürich, Zürich 8093, Switzerland; Laboratory for Advanced Analytical Technologies, Empa, Swiss Federal Laboratories for Materials Science and Technology, Dübendorf 8600, Switzerland; [orcid.org/0000-0003-2078-137X](https://orcid.org/0000-0003-2078-137X); Email: [jing.wang@ifu.baug.ethz.ch](mailto:jing.wang@ifu.baug.ethz.ch)

### Authors

Jiukai Tang – Institute of Environmental Engineering, ETH Zürich, Zürich 8093, Switzerland; Laboratory for Advanced Analytical Technologies, Empa, Swiss Federal Laboratories for Materials Science and Technology, Dübendorf 8600, Switzerland

Guangyu Qiu – Institute of Environmental Engineering, ETH Zürich, Zürich 8093, Switzerland; Laboratory for Advanced Analytical Technologies, Empa, Swiss Federal Laboratories for Materials Science and Technology, Dübendorf 8600, Switzerland; School of Biomedical Engineering, Shanghai Jiao Tong University, Shanghai 200240, China

Xiaobao Cao – Institute of Chemical and Bioengineering, ETH Zürich, Zürich 8093, Switzerland; Guangzhou Lab, International Bio Island, Guangzhou 510005 Guangdong, China

Andrew deMello – Institute of Chemical and Bioengineering, ETH Zürich, Zürich 8093, Switzerland; [orcid.org/0000-0003-1943-1356](https://orcid.org/0000-0003-1943-1356)

Complete contact information is available at: <https://pubs.acs.org/doi/10.1021/acssensors.2c01901>

### Author Contributions

J.T. conceived the idea and implemented all experiments. G.Q. assisted in establishing the optical system and provided suggestions. C.X. provided assistance in the COMSOL simulation. A.D. and J.W. provided comments. J.T., A.D., and J.W. wrote the manuscript. J.W. supervised this work.

## Notes

The authors declare no competing financial interest.

## REFERENCES

- (1) Atencia, J.; Beebe, D. J. Controlled microfluidic interfaces. *Nature* **2005**, *437*, 648–655.
- (2) Thorsen, T.; Roberts, R. W.; Arnold, F. H.; Quake, S. R. Dynamic Pattern Formation in a Vesicle-Generating Microfluidic Device. *Phys. Rev. Lett.* **2001**, *86*, 4163–4166.
- (3) Kuczenski, B.; LeDuc, P. R.; Messner, W. C. Pressure-driven spatiotemporal control of the laminar flow interface in a microfluidic network. *Lab Chip* **2007**, *7*, 647–649.
- (4) Kenis, P. J. A.; Ismagilov, R. F.; Whitesides, G. M. Microfabrication inside capillaries using multiphase laminar flow patterning. *Science* **1999**, *285*, 83–85.
- (5) Jeong, W.; Kim, J.; Kim, S.; Lee, S.; Mensing, G.; Beebe, D. J. Hydrodynamic microfabrication via “on the fly” photopolymerization of microscale fibers and tubes. *Lab Chip* **2004**, *4*, 576–580.
- (6) Park, J. U.; Meitl, M. A.; Hur, S. H.; Usrey, M. L.; Strano, M. S.; Kenis, P. J.; Rogers, J. A. In Situ Deposition and Patterning of Single-Walled Carbon Nanotubes by Laminar Flow and Controlled Flocculation in Microfluidic Channels. *Angew. Chem., Int. Ed.* **2006**, *45*, 581–585.
- (7) Paulsen, K. S.; Di Carlo, D.; Chung, A. J. Optofluidic fabrication for 3D-shaped particles. *Nat. Commun.* **2015**, *6*, No. 6976.
- (8) Takayama, S.; McDonald, J. C.; Ostuni, E.; Liang, M. N.; Kenis, P. J.; Ismagilov, R. F.; Whitesides, G. M. Patterning cells and their environments using multiple laminar fluid flows in capillary networks. *Proc. Natl. Acad. Sci. U.S.A.* **1999**, *96*, 5545–5548.
- (9) Zhao, H. T.; Zhang, Y.; Liu, P. Y.; Yap, P. H.; Ser, W.; Liu, A. Q. Chemical reaction monitoring via the light focusing in optofluidic waveguides. *Sens. Actuators, B* **2019**, *280*, 16–23.
- (10) Xiong, S.; Liu, A. Q.; Chin, L. K.; Yang, Y. An optofluidic prism tuned by two laminar flows. *Lab Chip* **2011**, *11*, 1864–1869.
- (11) Clement, C. E.; Thio, S. K.; Park, S.-Y. An optofluidic tunable Fresnel lens for spatial focal control based on electrowetting-on-dielectric (EWOD). *Sens. Actuators, B* **2017**, *240*, 909–915.
- (12) Fang, C.; Dai, B.; Xu, Q.; Zhuo, R.; Wang, Q.; Wang, X.; Zhang, D. Hydrodynamically reconfigurable optofluidic microlens with continuous shape tuning from biconvex to biconcave. *Opt. Express* **2017**, *25*, 888–897.
- (13) Oraie, M.; Latifi, H. Real-time refractive-index sensing by using liquid core/liquid cladding optofluidic waveguide. *Opt. Laser Technol.* **2019**, *111*, 303–306.
- (14) Sudarsan, A. P.; Ugaz, V. M. Multivortex micromixing. *Proc. Natl. Acad. Sci. U.S.A.* **2006**, *103*, 7228–7233.
- (15) Di Carlo, D. Inertial microfluidics. *Lab Chip* **2009**, *9*, 3038–3046.
- (16) Yang, Y.; Liu, A. Q.; Chin, L. K.; Zhang, X. M.; Tsai, D. P.; Lin, C. L.; Lu, C.; Wang, G. P.; Zheludev, N. I. Optofluidic waveguide as a transformation optics device for lightwave bending and manipulation. *Nat. Commun.* **2012**, *3*, No. 651.
- (17) Yang, Y.; Liu, A. Q.; Lei, L.; Chin, L. K.; Ohl, C. D.; Wang, Q. J.; Yoon, H. S. A tunable 3D optofluidic waveguide dye laser via two centrifugal Dean flow streams. *Lab Chip* **2011**, *11*, 3182–3187.
- (18) Ouano, A. C. Diffusion in Liquid Systems. I. A Simple and Fast Method of Measuring Diffusion Constants. *Ind. Eng. Chem. Fundam.* **1972**, *11*, 268–271.
- (19) Convery, N.; Gadegaard, N. 30 years of microfluidics. *Micro Nano Eng.* **2019**, *2*, 76–91.
- (20) Fan, X.; White, I. M. Optofluidic microsystems for chemical and biological analysis. *Nat. Photonics* **2011**, *5*, 591–597.
- (21) Seki, A.; Narita, K.; Watanabe, K. Refractive Index Measurement in Sucrose Solution and Beverage Using Surface Plasmon Resonance Sensor Based on Hetero-core Structured Fiber Optic. *Procedia Chem.* **2016**, *20*, 115–117.
- (22) Chen, J.; Guo, W.; Xia, M.; Li, W.; Yang, K. In situ measurement of seawater salinity with an optical refractometer based on total internal reflection method. *Opt. Express* **2018**, *26*, 25510–25523.
- (23) Qian, Y.; Zhao, Y.; Wu, Q. I.; Yang, Y. Review of salinity measurement technology based on optical fiber sensor. *Sens. Actuators, B* **2018**, *260*, 86–105.
- (24) Muchtaridi, M.; Musfiroh, I.; Hambali, N. N.; Indrayati, W. Determination of alcohol contents of fermented black tape ketan based on different fermentation time using specific gravity, refractive index and GC-MS methods. *J. Microbiol., Biotechnol. Food Sci.* **2020**, 933–946.
- (25) Tang, J.; Qiu, G.; Wang, J. Recent Development of Optofluidics for Imaging and Sensing Applications. *Chemosensors* **2022**, *10*, No. 15.
- (26) Zhu, J.; Han, G.; Hu, X.; Zuo, Y.; Chen, L.; Wang, F.; Yang, Y.; Jiang, F.; Sun, C.; Zhao, W.; Han, X. A Portable and Accurate Phosphate Sensor Using a Gradient Fabry–Pérot Array. *ACS Sens.* **2020**, *5*, 1381–1388.
- (27) Wang, F.; Zhu, J.; Hu, X.; Chen, L.; Zuo, Y.; Yang, Y.; Jiang, F.; Sun, C.; Zhao, W.; Han, X. Rapid nitrate determination with a portable lab-on-chip device based on double microstructured assisted reactors. *Lab Chip* **2021**, *21*, 1109–1117.
- (28) Wu, C.; Tse, M. L. V.; Liu, Z.; Guan, B.-O.; Zhang, A. P.; Lu, C.; Tam, H.-Y. In-line microfluidic integration of photonic crystal fibres as a highly sensitive refractometer. *Analyst* **2014**, *139*, 5422–5429.
- (29) Luo, Y.; et al. Optofluidic glucose detection by capillary-based ring resonators. *Opt. Laser Technol.* **2014**, *56*, 12–14.
- (30) Michel, D.; Xiao, F.; Alameh, K. A compact, flexible fiber-optic Surface Plasmon Resonance sensor with changeable sensor chips. *Sens. Actuators, B* **2017**, *246*, 258–261.
- (31) Flores, R.; Janeiro, R.; Viegas, J. Optical fibre Fabry–Pérot interferometer based on inline microcavities for salinity and temperature sensing. *Sci. Rep.* **2019**, *9*, No. 9556.
- (32) Weber, E.; Vellekoop, M. J. Optofluidic micro-sensors for the determination of liquid concentrations. *Lab Chip* **2012**, *12*, 3754–3759.
- (33) Tang, J.; Qiu, G.; Zhang, X.; Wang, J. A 3D-cascade-microlens optofluidic chip for refractometry with adjustable sensitivity. *Lab Chip* **2021**, *21*, 3784–3792.
- (34) Saetear, P.; Chamieh, J.; Kammer, M. N.; Manuel, T. J.; Biron, J. P.; Bornhop, D. J.; Cottet, H. Taylor Dispersion Analysis of Polysaccharides Using Backscattering Interferometry. *Anal. Chem.* **2017**, *89*, 6710–6718.
- (35) Tang, J.; Qiu, G.; Cao, X.; Yue, Y.; Zhang, X.; Schmitt, J.; Wang, J. Self-aligned 3D microlenses in a chip fabricated with two-photon stereolithography for highly sensitive absorbance measurement. *Lab Chip* **2020**, *20*, 2334–2342.
- (36) Tang, J.; Cao, X.; Qiu, G.; deMello, A.; Wang, J. Optical-Switch-Enabled Microfluidics for Sensitive Multichannel Colorimetric Analysis. *Anal. Chem.* **2021**, *93*, 6784–6791.
- (37) Campagnolo, L.; Nikolić, M.; Perchoux, J.; Lim, Y. L.; Bertling, K.; Loubière, K.; Prat, L.; Rakić, A. D.; Bosch, T. Flow profile measurement in microchannel using the optical feedback interferometry sensing technique. *Microfluid. Nanofluid.* **2013**, *14*, 113–119.
- (38) Urréjola, S.; Sánchez, A.; Hervello, M. F. Refractive Indices of Lithium, Magnesium, and Copper (II) Sulfates in Ethanol–Water Solutions. *J. Chem. Eng. Data* **2010**, *55*, 482–487.
- (39) Dan-Feng, L.; Zhi-Mei, Q. Glass/Ta<sub>2</sub>O<sub>5</sub> Composite Waveguides for Application as an Integrated Polarimetric Interferometer. *Chin. Phys. Lett.* **2010**, *27*, No. 104206.
- (40) Guggenheim, E. A. The diffusion coefficient of sodium chloride. *Trans. Faraday Soc.* **1954**, *50*, 1048–1051.
- (41) Smith, I. E.; Storrow, J. A. Diffusion coefficients of ethanol in aqueous solutions. *J. Appl. Chem.* **2007**, *2*, 225–235.
- (42) Robinson, R.; Chia, C. The diffusion coefficient of calcium chloride in aqueous solution at 25°. *J. Am. Chem. Soc.* **1952**, *74*, 2776–2777.
- (43) Gosting, L. J.; Akeley, D. F. A Study of the Diffusion of Urea in Water at 25 with the Gouy Interference Method. *J. Am. Chem. Soc.* **1952**, *74*, 2058–2060.



- (44) Harned, H. S.; Hudson, R. M. The diffusion coefficient of magnesium sulfate in dilute aqueous solution at 25°. *J. Am. Chem. Soc.* **1951**, *73*, 5880–5882.
- (45) Gage, J. C. A cell for the measurement of diffusion in aqueous solution. *Trans. Faraday Soc.* **1948**, *44*, 253–256.
- (46) Harned, H. S.; Nuttall, R. L. The diffusion coefficient of potassium chloride in dilute aqueous solution. *J. Am. Chem. Soc.* **1947**, *69*, 736–740.
- (47) Scott, T. A. Refractive Index of Ethanol–Water Mixtures and Density and Refractive Index of Ethanol–Water–Ethyl Ether Mixtures. *J. Phys. Chem. A* **1946**, *50*, 406–412.
- (48) Tan, C. H.; Huang, X. G.; Shi, Y. P. In situ measurements of the solubilities of salt–water systems by a fiber sensor. *Rev. Sci. Instrum.* **2009**, *80*, No. 034103.
- (49) Hall, J. R.; Wishaw, B. F.; Stokes, R. H. The Diffusion Coefficients of Calcium Chloride and Ammonium Chloride in Concentrated Aqueous Solutions at 25°. *J. Am. Chem. Soc.* **1953**, *75*, 1556–1560.
- (50) Xie, N.; Zhang, H.; et al. In-Line Microfiber-Assisted Mach–Zehnder Interferometer for Microfluidic Highly Sensitive Measurement of Salinity. *IEEE Sens. J.* **2018**, *18*, 8767–8772.
- (51) Walton, N. R. G. Electrical Conductivity and Total Dissolved Solids-What is Their Precise Relationship? *Desalination* **1989**, *72*, 275–292.

## Recommended by ACS

### Programmable Droplet Microfluidics Based on Machine Learning and Acoustic Manipulation

Kyriacos Yiannacou, Veikko Sariola, *et al.*

SEPTEMBER 13, 2022  
LANGMUIR

READ 

### Light-Driven Liquid Conveyors: Manipulating Liquid Mobility and Transporting Solids on Demand

Kengo Manabe, Yasuo Norikane, *et al.*

OCTOBER 12, 2022  
ACS NANO

READ 

### Trapping of Aqueous Droplets under Surface Acoustic Wave-Driven Streaming in Oil-Filled Microwells

A. Nath, A. K. Sen, *et al.*

APRIL 08, 2022  
LANGMUIR

READ 

### Oscillation-Induced Mixing Advances the Functionality of Liquid Marble Microreactors

Xianglong Pang, Xiaoguang Li, *et al.*

FEBRUARY 16, 2022  
ACS APPLIED MATERIALS & INTERFACES

READ 

Get More Suggestions >